Energy cascade in a homogeneous swarm of bubbles rising in a vertical channel

By **C. C. K. Lai**†, **B. Fraga**‡, **W. R. H. Chan** AND **M. S. Dodd**

We perform direct numerical simulations (DNS) of millimeter-size air bubbles rising in a vertical water channel. Our objective is to study the energy cascade in this simple configuration, which is a prototype of other more complex flows involving bubbles and droplets. Both rigid and deformable bubbles are considered using the immersed boundary method (IBM) and the volume of fluid (VoF) method. The energy cascade is quantified using the nonlinear interscale energy transfer term appearing in the Kármán-Howarth-Monin (K-H-M) equation. We observe that the energy cascade is highly anisotropic in scale space with vertical turbulent eddies exhibiting strong inverse cascades. When scale-normalized, the interscale energy transfer term shows a plateau for turbulent eddies whose size is approximately 1 to 2 bubble diameters. However, the magnitude of that term is only 50–60% of the required viscous dissipation, indicating that the classic forward-cascade picture by Richardson and Kolmogorov is not satisfied despite the existence of a scale-invariant range.

1. Introduction

Examples of turbulent two-phase flows involving millimeter-sized droplets and particles are abundant in the natural and human-made environment. Intensive experimental and numerical studies done in the past two decades have improved our understanding of (1) the modulation of continuous-phase turbulence (Balachandar & Eaton 2010), (2) the transition between different flow regimes (Capecelatro *et al.* 2018), (3) the enhancement of turbulent mixing brought by the dispersed phase, and (4) the collective effects of particle wakes (Riboux *et al.* 2013). Despite these efforts, a fundamental aspect of fluid turbulence – the energy cascade – has received less attention. The cascade refers to the transfer of kinetic energy among turbulent eddies of different sizes. In the classic, forward-cascading, Richardson-Kolmogorov (R-K) phenomenology, kinetic energy is passed down from the energy-containing (large) eddies to the viscous dissipative (small) eddies through the inertial subrange. Eddies within the inertial subrange only passively transfer the received energy to smaller ones. This postulate is asserted to be true for arbitrary turbulent flows at sufficiently high Reynolds number (Pope 2000) and leads to the famous $-5/3$ spectral slope scaling in the spatial-temporal spectra of velocity fluctuations (Obukhov 1941). The existence of an inertial subrange has been shown in previous research for various flows by plotting the scale-normalized interscale energy transfer rate as a function of the eddy size (i.e. scale); a plateau appears for the subrange. However, the appearance of a $-5/3$ scaling in the spectra does not imply an inertial subrange. Recent studies of the production region of turbulent kinetic energy (TKE) behind fractal grids (Gomes-Fernandes *et al.* 2015) demonstrate that such scaling is also present in this highly non-homogeneous, non-isotropic region where the second similarity hypothesis by Kolmogorov

---

† Physics Division, Los Alamos National Laboratory
‡ School of Civil Engineering, University of Birmingham, UK

does not hold (Pope 2000). Eddies with a particular set of orientations can exhibit an inverse energy cascade, and therefore they deviate from the R-K picture.

The picture of energy cascade in general two-phase flows is not clear. This is because the dispersed phase is another source of TKE in addition to the production by fluid mean shear (Pope 2000). The scales over which this extra production source occurs are limited by the characteristic size of the dispersed phase, e.g., diameters of bubbles. Depending on the ratio between these scales and those of the fluid turbulence, different interactions can occur in the cascade of energy. For millimeter-sized air bubbles rising in water, the -3 (or $-8/3$) spectral slope has been shown to be a robust feature of the fluid-phase velocity spectra since the original study on homogeneous bubble swarms in a vertical channel by Lance & Bataille (1991). These authors reasoned such scaling by stating the balance between the production by bubbles and dissipation in the spectral energy equation; the spectral energy transfer term was neglected. Physically, this means that energy does not go through a cascade and is dissipated immediately by viscosity. This is a dramatic departure from the R-K phenomenology, which has not been demonstrated in the scale space. Recently, the -3 spectral slope was also shown to exist in bubbly flows with background fluid turbulence by Prakash *et al.* (2016) and Almeras *et al.* (2017).

Our objectives are to answer the following three questions: Does an inertial subrange exist in bubbly flows? Is the Lance & Bataille (1991) reasoning for the appearance of -3 spectral slope right? What is the map of interscale energy transfer in bubbly flows? To answer these questions, we apply the von Kármán-Howarth-Monin (K-H-M) equation (Hill 2002) to a set of direct numerical simulations (DNS) of homogeneous bubble swarms rising in a vertical channel. The K-H-M equation tracks the spatial-temporal evolution of the two-point, second-order velocity structure function in which the structure function has the interpretation of kinetic energy possessed by a turbulent eddy of a given scale (size) (Davidson 2015). Hence, we can study the interscale energy transfer in bubbly flows. We consider an initially quiescent fluid because we want to isolate the effects of bubbles on the energy cascade independently from any background fluid turbulence.

2. Mathematical description

2.1. *Governing equations*

The dynamics of the liquid matrix or continuous phase are predicted through DNS of the Navier-Stokes equations for an unsteady, incompressible and viscous flow, expressed as follows

$$\nabla \cdot \mathbf{u} = 0, \tag{2.1a}$$

$$\frac{\partial \mathbf{u}}{\partial t} + \mathbf{u} \cdot \nabla \mathbf{u} = -\frac{1}{\rho} \nabla p + \nu \nabla^2 \mathbf{u} + \mathbf{f}, \tag{2.1b}$$

where $\mathbf{u} = \mathbf{u}(\mathbf{x}, t)$ is the fluid velocity, ρ is the density, $p = p(\mathbf{x}, t)$ is the scalar pressure field, ν is the water's kinematic viscosity, and $\mathbf{f} = \mathbf{f}(\mathbf{x}, t)$ is the body force term exerted at the bubble-liquid interface. We adopt two fundamentally different approaches to simulating the dispersed phase, which result in different ways of calculating $\mathbf{f}$.

2.2. *Eulerian-Lagrangian model*

The Eulerian-Lagrangian code discretizes both the diffusive and convective terms by second-order central difference schemes, whereas a three-step Runge-Kutta algorithm is adopted for the time derivatives. The solver is based on a predictor-corrector method in which a multigrid algorithm solves the Poisson equation for the pressure field. This code had previously been validated successfully for bubbly flows simulations using point-particle Eulerian-Lagrangian methods (Fraga *et al.* 2016) and for fluid-structure interaction problems using the immersed boundary method (IBM) (Chua *et al.* 2019).

The discrete phase is composed of spherical non-deformable gas bubbles defined by the position and velocity vectors of their centroids. The Eulerian-Lagrangian model does not account for the effect of collisions between bubbles, assuming a low a void fraction and a significant presence of surfactant ("dirty" bubble) that prevents coalescence. The effect of shape deformation and bubble-bubble interaction is only considered in volume-of-fluid (VoF) simulations (Section 2.3). The motion of the bubble centroid is governed by

$$m_b \frac{d\mathbf{u_b}}{dt} = \rho_l \int_S \mathbf{T} dS + (\rho_b - \rho_l) V_b \mathbf{g}, \tag{2.2}$$

where m_b is the bubble mass, $\mathbf{u_b} = \mathbf{u_b}(t)$ is the Lagrangian velocity at the bubble centroid, ρ_l and ρ_b are the water and air densities, respectively, V_b is the bubble's volume, $\mathbf{g}$ is the gravity acceleration, and $\int_S \mathbf{T} dS = \int_S \left[-(\nabla p)/\rho_l + \nu \nabla^2 \mathbf{u} \right] dS$ is the integral of the hydrodynamic stress tensor $\mathbf{T}$ around the bubble's surface, which is approximated using an implementation of the IBM (Peskin 2002; Uhlmann 2005; Schwarz *et al.* 2015). The spherical interface of each bubble is composed of a collection of N_L Lagrangian markers, which force a no-slip boundary condition on the bubble surface. At every time step, the position and velocity Lagrangian vectors are distributed among the message-passing interface blocks using an algorithm based on work by Ouro *et al.* (2019). The preliminary Eulerian velocity vector field $\tilde{\mathbf{u}}$, unaffected by the bubble presence, is interpolated using third-order delta functions (Yang *et al.* 2009) at each Lagrangian location as

$$\mathbf{U}_L = \sum_{i=1}^{n_E} \tilde{\mathbf{u}}_i \cdot \delta(\mathbf{x}_i - \mathbf{X}_L) \Delta \mathbf{V}_E, \tag{2.3}$$

where $\mathbf{U}_L$ is the interpolated Eulerian velocity at the Lagrangian location $\mathbf{X}_L$, $\mathbf{x}_i$ is the Eulerian position vector, n_E the number of Eulerian neighbouring nodes, $\Delta \mathbf{V}_E$ is the cell volume, and δ is the interpolation delta function. Once the Eulerian velocities are mapped into the Lagrangian framework, a force vector $\mathbf{F}_L = (\mathbf{u}_b^{t-1} - \mathbf{U}_L)/\Delta t$ is calculated explicitly for every Lagrangian marker. By integrating all the forces across the bubble interface, we approximate the value of $\int_S \mathbf{T} dS$, which is gathered for every bubble by the master processor. The bubble centroid velocity is obtained by implicitly solving Eq. (2.2). Once the bubble centroids' positions are updated, the bubble-to-liquid coupling is achieved by calculating the forcing term $\mathbf{f}$ at every Eulerian node within range (defined by the delta function's stencil) of the bubble as

$$\mathbf{f}_i = \sum_{L=1}^{n_L} \frac{\mathbf{U}_L - \mathbf{u}_b^t}{\Delta t} \delta(\mathbf{X}_L - \mathbf{x}_i) \Delta V_L, \tag{2.4}$$

where $\mathbf{f}_i$ is the contribution to the momentum balance of the Eulerian node i by n_L Lagrangian neighbors, Δt is the time step, and ΔV_L is the volume of influence of each Lagrangian marker. This forcing term is used to correct the preliminary velocities before applying the multigrid solver, which will ensure mass conservation and provide the definitive Eulerian velocity field.

2.3. *Volume of fluid model*

In the VoF method, the sharp interface between two immiscible fluids is determined using the VoF color function, C, which represents the volume fraction of the gas in each computational cell. We solve the governing equations, Eqs. (2.1*a*)-(2.1*b*), throughout the whole computational domain, including the interior of the bubbles. The governing equations are discretized in space in an Eulerian framework using the second-order central difference scheme on a uniform staggered mesh.

A body force has been added in the direction of gravity to ensure that the net momentum flux in the vertical direction is zero (i.e., to prevent uniform acceleration of both fluids). This modification has been used by other groups to simulate droplets and bubbles in periodic, vertical channels (Gueyffier *et al.* 1999; Bunner & Tryggvason 2002). In the VoF approach, the source term in Eq. (2.1*b*) is $\mathbf{f}_\sigma = \mathbf{f}_\sigma(\mathbf{x}, t)$, the surface tension force, which is computed by using Brackbill et al.'s (1992) continuum surface force approach as

$$\mathbf{f}_\sigma = \frac{\rho}{\bar{\rho}}\kappa\nabla C, \tag{2.5}$$

where $\bar{\rho} \equiv (\rho_1 + \rho_2)/2$. The interface curvature κ^{n+1} is computed using the height-function method (Cummins *et al.* 2005) with improvements developed by López *et al.* (2009). The equations are integrated in time using the second-order Adams-Bashforth scheme, and the pressure is computed by solving the Poisson equation (Dodd & Ferrante 2014) for which a combination of a two-dimensional fast Fourier transforms (FFT) in the x–y plane and Gauss elimination in the z-direction (Schmidt *et al.* 1984) is used. This FFT-based method is 10–40 times faster than the standard multigrid-based pressure-correction method (Dodd & Ferrante 2014).

In our VoF method, the interface between the two fluids is reconstructed using a piecewise linear interface calculation (Youngs 1982). The volume fraction C is advanced in time using the Eulerian implicit–Eulerian algebraic–Lagrangian explicit (EI-EA-LE) algorithm originally proposed by Scardovelli *et al.* (2002) and later improved by Baraldi *et al.* (2014) to ensure local and global mass conservation. Using the improved EI-EA-LE algorithm, the cell-centered volume fraction C is advected using the face-centered velocity field $\mathbf{u}$. The method displays second-order spatial accuracy for values of Courant-Friedrichs-Lewy number ≤ 0.1. Furthermore, the average geometrical error ($E_g = |C(\mathbf{x}) - C_{\text{exact}}(\mathbf{x})|$) is less than 1 % for a moving droplet with 30 grid cells or more across the diameter. The complete description of the method and the results are reported by Baraldi *et al.* (2014). Breakup and coalescence of fluid volumes are handled implicitly by the VoF method. For example, if two interfaces occupy the same computational cell during the VoF update from time level n to $n + 1$, then the two VoF volumes are merged (or coalesced) automatically. Likewise, when the thickness of a bubble ligament falls below the grid spacing, h, it will break.

3. Results

We simulated bubbly flows in a periodic vertical channel filled with initially quiescent water. The bubble initial diameter is $D_0 = 2$ mm, providing $Re_p \approx 400$, and the channel dimensions are $40D_0 \times 20D \times 20D_0$. The gravity acceleration is $\mathbf{g} = -9.81$ ms^{-2}. A void fraction of 0.5% was simulated for VoF, and 0.5% and 0.25% for IBM. Unless stated differently, all the results shown correspond to a void fraction $\alpha = 0.5\%$. The grid resolution for VoF is approximately 13 grid points per D_0, whereas it is 8 Eulerian

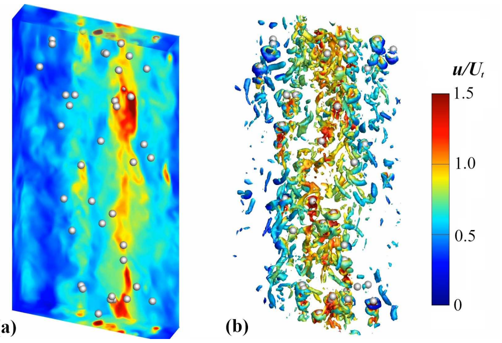

FIGURE 1. (a) Instantaneous Eulerian (liquid phase) velocity field and (b) vortex tubes at the bubbles' wakes at the same time instant predicted by the IBM 0.5% void fraction DNS. The velocity is scaled with the bubble terminal velocity U_t and the vortex tubes are visualised using Q criterion.

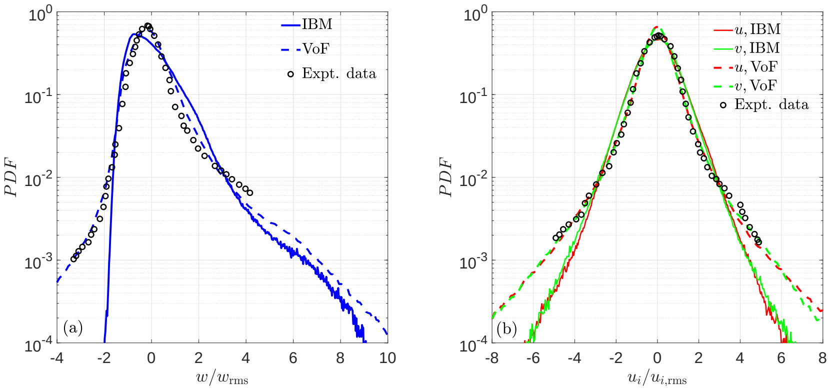

FIGURE 2. PDFs of the standardized velocity fluctuations $u_i/u_{i,\rm rms}$: (a) vertical velocity w and (b) horizontal velocities (u, v). The experimental data are from homogeneous bubble swarms reported by Risso (2018).

cells for IBM, yielding 210 Lagrangian markers per bubble. Figure 1 shows a snapshot of the domain with the instantaneous Eulerian velocity field (left) and the Q criterion isosurfaces describing the vortex tubes generated at the boundary layers and wakes of the air bubbles (right) for the IBM DNS with a 0.5% void fraction.

Figure 2 shows the probability density functions (PDFs) of the standardized velocity fluctuations $u_i/u_{i,\rm rms}$ calculated from both simulation approaches. This standardization facilitates the comparison among flows with different void fractions and, hence, different magnitudes of kinetic energy of the induced liquid fluctuations. The figure is also plotted with a semi-log ordinate axis to show the stretched exponential tails of the PDFs (Risso 2018); PDFs having the form $p(x) \sim \exp(-|x|)$ appear as straight lines in such a plot. Figure 2 shows key features of the velocity PDFs found from experiments are reproduced by both simulation approaches: (1) only the w-PDF is left-skewed with a long postive tail, whereas the PDFs of u and v are symmetric about zero, (2) the mode of w is negative, and (3) all PDFs have stretched exponential tails. The long positive tails of w have been shown to be caused by the near wake (within two bubble diameters) behind the rising bubbles (Almeras *et al.* 2017; Risso 2018), and their appearance means that large upward velocities occur more frequently than downward ones with the same magnitude.

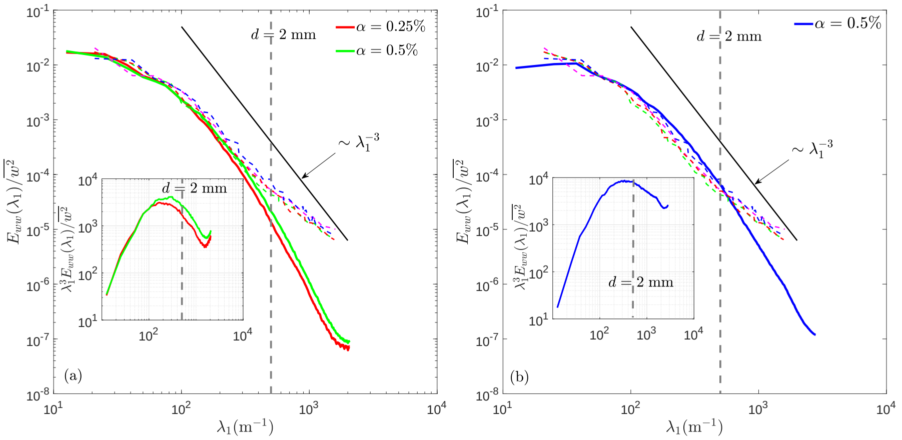

FIGURE 3. Vertical (one-dimensional) spectra of the vertical velocity fluctuations $E_{ww}(\lambda_1)$: (a) IBM and (b) VoF method. The solid lines are results from present DNS simulations, while the dashed lines are experimental data extracted from Risso (2018).

Apart from the similarities, it is interesting to see that the PDFs computed from the VoF dataset deviate from those of IBM for large velocity fluctuations, and they are also in better agreement with the experimental data. A plausible explanation is that the bubbles are deformable and can undergo coalescence/breakup in the VoF simulations. These processes create large strains across the fluid-bubble interface, and therefore higher magnitudes of velocity fluctuations can be expected in the PDFs. The same is ruled out in the IBM approach, where bubbles are modeled as moving solid boundaries within the fluid. We note that the bubbles in the experiments could deform but did not coalescence or break up. This indicates that deformability is mostly responsible for the good agreement between the results of VoF and experiments.

Figure 3 shows the one-dimensional velocity spectra $E_{ww}(\lambda_1)$ in both uncompensated and compensated (insets) formats. The experimental data (dashed lines) derived from swarms of 2.5-mm-diameter bubbles and with a void fraction between 0.5 and 7% are included for comparison. Both simulation approaches produce velocity spectra very similar to the ones measured for $\lambda_1 < 500\ \mathrm{m}^{-1}$; this inverse length scale corresponds to the $D_0 = 2$ mm used in the simulations. The characteristic -3 spectral slope observed in bubbly flows (Almeras *et al.* 2017; Risso 2018) is found in the range $100\ \mathrm{m}^{-1} < \lambda_1 < 500\ \mathrm{m}^{-1}$. Beyond $500\ \mathrm{m}^{-1}$, the spectra from the simulations decay faster than reported from experiments. This is most likely due to inherent noise with the measurement technique and to the coarser spatial resolution in the experiments. From this comparison, we conclude that the deformability of bubbles is not crucial to produce the -3 spectral slope as the scales associated with the deformation of bubbles are smaller than the bubble diameter. Also, we conjecture that the special -3 scaling is related to wake-to-wake interactions that involve scales larger than the bubble diameter.

Figure 4 shows the joint PDF of the second Q and third R invariants of the velocity gradient tensor (Meneveau 2011). Interestingly, the IBM results closely resemble those reported for many single-phase turbulent flows; i.e., a Vieillefosse tail and a rich (with high probabilities) enstrophy amplification quadrant ($Q > 0$ and $R < 0$), whereas the VoF results exhibit a depletion (low probabilities) in both of the enstrophy amplification and destruction quadrants ($Q > 0$ and $R > 0$). The vortex-stretching mechanism (the

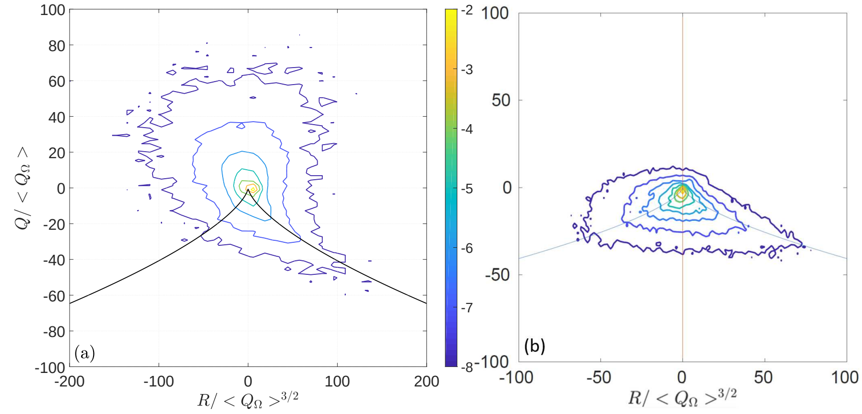

FIGURE 4. Joint PDF of the second Q and third R invariants of the velocity gradient tensor $\partial u_i/\partial x_j$: (a) IBM and (b) VoF method. The black solid line represents $0 = Q^3 + 27R^2/4$, and it demarcates swirling regions (above) from straining regions (below). Starting from the outermost contour, the contour values increase from -8 inwards at a fixed interval of -1.

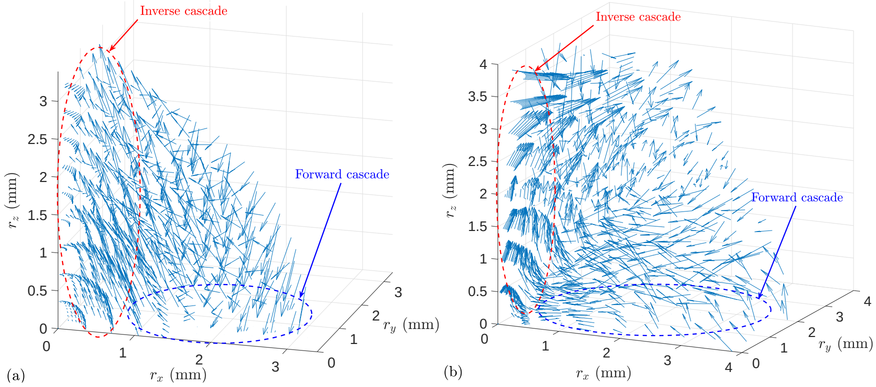

FIGURE 5. Ensemble averaged map of the nonlinear interscale energy flux term $\Pi(r_x, r_y, r_z) = \partial\overline{\delta u_k \delta q^2}/\partial r_k$: (a) IBM and (b) VoF method

enstrophy production $\omega_i S_{ij} \omega_j$ term appearing in the σ^2-equation) is the sole inviscid mechanism often interpreted to be responsible for energy cascade (Tsinober 2009). The depletion of it in the simulation of deformable bubbles suggests that the transfer of fluid kinetic energy from one scale to another is accomplished by a different means than the known vortex-stretching mechanism.

Figure 5 shows the ensemble-averaged nonlinear interscale energy flux term Π in the K-H-M equation. This term quantifies the magnitude and the direction of interscale energy transfer at a scale $|\mathbf{r}|$ and hence, the energy cascade. We have chosen to compute this term for $|\mathbf{r}|$ in the range 0–4 mm, which corresponds to inverse length scales $\lambda_1 \geq 250$ m^{-1} in Figure 3. This λ_1 range includes the -3 spectral slope and the subsequent viscous dissipation range that is relevant to the study of energy cascade in our bubbly flows. For spatially homogeneous flows, $\Pi = \Pi(r_x, r_y, r_z)$ is only a function of the separation vector $\mathbf{r} = \mathbf{x}' - \mathbf{x} = r_x\mathbf{i} + r_y\mathbf{j} + r_z\mathbf{k}$ between any two spatial points. The results shown in the figure were computed using 0.4% of the available data points in the computational domain. This

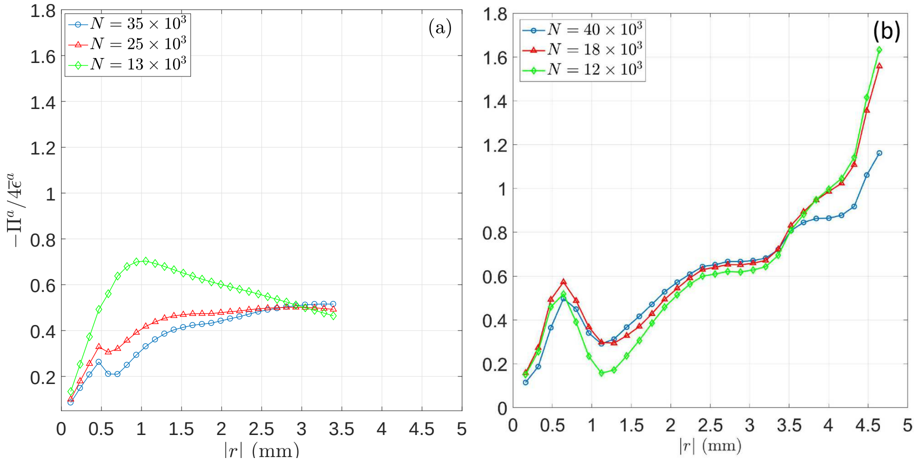

FIGURE 6. Spherically averaged nonlinear interscale energy flux term $-\Pi^a/4\bar{\epsilon}^a$ as a function of eddy size $r = \sqrt{r_x^2 + r_y^2 + r_z^2}$: (a) IBM and (b) VoF method.

level of data utilization seemed to produce a converged spherically averaged interscale energy flux (see Figure 6); more rigorous convergence tests will be done in the future. Figure 5 shows that both simulation methodologies produce strong inverse cascade for eddies predominantly aligned to the vertical (arrows pointing away from the origin with values of r_x and r_y close to zero). The horizontally aligned eddies (with small values of r_z) exhibit a forward cascade (arrows pointing toward the origin). There are structural differences in Π between the two simulations, but both share the same features.

To provide an integrated view of the energy cascade, Figure 6 shows the spherically averaged Π term: $-\Pi^a/4\bar{\epsilon}^a$. The averaging removes the dependence of Π on the different orientations of $\mathbf{r}$ and allows us to examine Π solely as a function of the size $|\mathbf{r}|$ of a turbulent eddy. This is important in practice because many turbulence models could only account for a net interscale energy flux but not the directionally dependent transfer. First, the VoF results seem to converge faster than the IBMs as the number of data points utilized, N, increases. Second, both methods show that $-\Pi^a/4\bar{\epsilon}^a$ initially increases from small values near $|\mathbf{r}| = 0$ to a local maximum at $|\mathbf{r}| = 0.5$ mm, and then decreases before increasing again to reach a plateau for scales in the range $|\mathbf{r}| = 2 - 3.5$ mm. In this plateauing range, the scale-normalized energy flux is between 0.5 and 0.6, which is less than the value of one demanded by the classic R-K forward-cascade phenomenology. The sudden decrease after $|\mathbf{r}| = 0.5$ mm could correspond to a range of scales where the vertically aligned eddies (inverse cascade) are more dominant, which is the case of the near-wake region. The differences between IBM and VoF on the length of this valley might be due to the differences in shape and size of the bubbles produced in both simulations.

4. Conclusions

We have successfully developed two DNS codes to study homogeneous bubbly flows in a vertical channel using the IBM and the VoF method. We found that both methods reproduce the characteristic -3 spectral slope in the one-dimensional velocity spectra and that deformability of bubbles plays a negligible role in this scaling. Deformability does, however, produce higher velocity fluctuations as observed in physical experiments, while IBM with its rigid bubble assumption fails to predict them. The energy cascade in bubbly flows is quantified using the nonlinear interscale energy transfer term Π appearing in the K-H-M equation. We observed that the energy cascade is highly anisotropic in scale space with vertical turbulent eddies exhibiting strong inverse cascades. When scale-normalized, the interscale energy transfer term shows a plateau for turbulent eddies that are 1–2 bubble diameters large. However, the magnitude is only 50–60% of the required viscous dissipation, indicating that the classic forward-cascade picture by Richardson and Kolmogorov is not satisfied despite the existence of a scale-invariant range. Finally, from an analysis of the QR-plots, we found that bubbly flows with deformable bubbles have much-weakened enstrophy production and destruction when compared with flows with rigid bubbles. As vortex stretching is the sole inviscid mechanism responsible for a forward energy cascade, this observation suggests that the interscale energy transfer in flows with deformable bubbles relies on a very different mechanism, which, will require new turbulence models.

Acknowledgments

The authors acknowledge use of computational resources from the Certainty cluster awarded by the National Science Foundation to CTR.

REFERENCES

Almeras, E., Mathai, V., Lohse, D. & Sun, C. 2017 Experimental investigation of the turbulence induced by a bubble swarm rising within incident turbulence. *J. Fluid Mech.* **825**, 1091–1112.

Balachandar, S. & Eaton, J. K. 2010 Turbulent dispersed multiphase flow. *Annu. Rev. Fluid Mech.* **42**, 111–133.

Baraldi, A., Dodd, M. S. & Ferrante, A. 2014 A mass-conserving volume-of-fluid method: Volume tracking and droplet surface-tension in incompressible isotropic turbulence. *Comput. Fluids* **96**, 322–337.

Brackbill, J., Kothe, D. & Zemach, C. 1992 A continuum method for modeling surface tension. *J. Comput. Phys.* **100**, 335–354.

Bunner, B. & Tryggvason, G. 2002 Dynamics of homogeneous bubbly flows. Part 1. Rise velocity and microstructure of the bubbles. *J. Fluid Mech.* **466**, 17–52.

Capecelatro, J., Desjardins, O. & Fox, R. 2018 On the transition between turbulent regimes in particle-laden channel flows. *J. Fluid Mech.* **845**, 499–519.

Chua, K. V., Fraga, B., Stoesser, T., Hong, S. & Sturm, T. 2019 Characterization of turbulent structures in the wake of bridge abutments of variable length. *J. Hydraul. Eng.* In press.

Cummins, S., Francois, M. & Kothe, D. 2005 Estimating curvature from volume fractions. *Comput. Struct.* **83**, 425–434.

Davidson, P. 2015 *Turbulence - An Introduction for Scientists and Engineers*. Oxford University Press.

Dodd, M. S. & Ferrante, A. 2014 A fast pressure-correction method for incompressible two-fluid flows. *J. Comput. Phys.* **273**, 416–434.

Fraga, B., Stoesser, T., Lai, C. C. & Socolofsky, S. A. 2016 A LES-based Eulerian–Lagrangian approach to predict the dynamics of bubble plumes. *Ocean Model.* **97**, 27–36.

Gomes-Fernandes, R., Ganapathisubramani, B. & Vassilicos, J. 2015 The energy cascade in near-field non-homogeneous non-isotropic turbulence. *J. Fluid Mech.* **771**, 676–705.

Gueyffier, D., Li, J., Nadim, A., Scardovelli, R. & Zaleski, S. 1999 Volume-of-fluid interface tracking with smoothed surface stress methods for three-dimensional flows. *J. Comput. Phys.* **152**, 423–456.

Hill, R. 2002 Exact second-order structure-function relationships. *J. Fluid Mech.* **468**, 317–326.

Lance, M. & Bataille, J. 1991 Turbulence in the liquid phase of a uniform bubbly air-water flow. *J. Fluid Mech.* **222**, 95–118.

López, J., Zanzi, C., Gómez, P., Zamora, R., Faura, F. & Hernández, J. 2009 An improved height function technique for computing interface curvature from volume fractions. *Method. Appl. M.* **198**, 2555–2564.

Meneveau, C. 2011 Lagrangian dynamics and models of the velocity gradient tensor in turbulent flows. *Annu. Rev. Fluid Mech.* **43**, 219–245.

Miller, G. H. & Colella, P. 2002 A conservative three-dimensional Eulerian method for coupled solid–fluid shock capturing. *J. Comput. Phys.* **183**, 26–82.

Obukhov, A. 1941 Energy distribution in the spectrum of a turbulent flow. *Izv. Akad. Nauk SSSR Ser. Geogr. Geofiz.* **4-5**, 453–466.

Ouro, P., Fraga, B., Lopez-Novoa, U. & Stoesser, T. 2019 Scalability of an eulerian-lagrangian large-eddy simulation solver with hybrid mpi/openmp parallelisation. *Comput. Fluids* **179**, 123-136.

Peskin, C. 2002 The immersed boundary method. *Acta Numerica* **11**, 1–39.

Pope, S. B. 2000 *Turbulent Flows*. Cambridge Univ. Press.

Prakash, V., Mercado, J., van Wijngaarden, L., Mancilla, E., Tagawa, Y., Lohse, D. & Sun, C. 2016 Energy spectra in turbulent bubbly flows. *J. Fluid Mech.* **791**, 174–190.

Riboux, G., Legendre, D. & Risso, F. 2013 A model of bubble-induced turbulence based on large-scale wake interactions. *J. Fluid Mech.* **719**, 362–387.

Risso, F. 2018 Agitation, mixing, and transfers induced by bubbles. *Annu. Rev. Fluid Mech.* **50**, 25–48.

Scardovelli, R., Aulisa, E., Manservisi, S. & Marra, V. 2002 A marker-VOF algorithm for incompressible flows with interfaces. In *Advances in Free Surface and Interface Fluid Dynamics*, , vol. 1, pp. 905–910. ASME Conf. Proc., Joint U.S.-European Fluids Engineering Division Conference.

Schmidt, H., Schumann, U. & Volkert, H. 1984 Three dimensional, direct and vectorized elliptic solvers for various boundary conditions. Rep. 84-15. DFVLR-Mitt.

Schwarz, S., Kempe, T. & Fröhlich, J. 2015 A temporal discretization scheme to compute the motion of light particles in viscous flows by an immersed boundary method. *J. Comput. Phys.* **281**, 591–613.

Tsinober, A. 2009 *An informal conceptual introduction to turbulence.* 2nd edn. Springer

Uhlmann, M. 2005 An immersed boundary method with direct forcing for the simulation of particulate flows. *J. Comput. Phys.* **209**, 448–476.

Yang, X., Zhang, X., Li, Z. & He, G.-W. 2009 A smoothing technique for discrete delta functions with application to immersed boundary method in moving boundary simulations. *J. Comput. Phys.* **228**, 7821–7836.

Youngs, D. L. 1982 Time-dependent multi-material flow with large fluid distortion. *Numer. Methods Fluid Dyn.* **1**, 41–51.